crystals

MDPI

Article

Study on the Laser Melting Procedure for the Specified Zone of the TC4 Titanium Alloy

Jian Han *, Shilong Jia, Yude Liu *, Wentian Shi, Yusheng Zhou, Yuxiang Lin, Jihang Li and Yifan Han

School of Artificial Intelligence, Beijing Technology and Business University, Beijing 100048, China; jia_shilong@163.com (S.J.); shiwt@th.btbu.edu.cn (W.S.); zhou_yusheng1998@163.com (Y.Z.); linyuxiang_123@163.com (Y.L.); q13366019655@126.com (J.L.); 13716968370@163.com (Y.H.)
* Correspondence: jianhan_bj@163.com (J.H.); liu_yude@126.com (Y.L.)

Abstract: This paper presents an in-depth study of the variable reference process to improve the organization and properties of selective laser melting TC4 specimens. A relationship equation between body energy density and stratification is proposed. This study aimed to look into how layer and volume energy density affect the surface, tensile characteristics, and microstructure of specimens. The test findings demonstrated that specimen densities rise as the power index falls, with the most excellent density reaching 99.42%. The number of secondary α′ phases declined as the energy density of the laminae slowed down. The tensile strength of these specimens reached 1190.84 MPa, and the yield strength came at 1103.87 MPa with the same interval of variable laser power. This offers a fresh avenue for research into SLM to enhance the specimens' overall performance.

Keywords: variable parameter forming; volume energy density; microstructure; Ti-6Al-4V; selective laser melting

check for updates

Citation: Han, J.; Jia, S.; Liu, Y.; Shi, W.; Zhou, Y.; Lin, Y.; Li, J.; Han, Y. Study on the Laser Melting Procedure for the Specified Zone of the TC4 Titanium Alloy. *Crystals* **2023**, *13*, 1041. https://doi.org/10.3390/cryst13071041

Academic Editor: Nan Kang

Received: 31 May 2023
Revised: 14 June 2023
Accepted: 19 June 2023
Published: 30 June 2023

Copyright: © 2023 by the authors. Licensee MDPI, Basel, Switzerland. This article is an open access article distributed under the terms and conditions of the Creative Commons Attribution (CC BY) license (https://creativecommons.org/licenses/by/4.0/).

1. Introduction

Selective laser melting is one of the most commonly used technologies for metal additive manufacturing. The laser selective melting of titanium alloys has been widely used for critical and complex components in many fields, such as aviation, aerospace, medical and biological implants, and it has a vital status and application prospects [1–4]. However, because of the complex SLM forming process, which involves metallurgical, physical, chemical, and material thermal coupling, its point-by-point, line-by-line, and surface-by-surface forming characteristics can result in the presence of inevitable defects in the parts, some of which significantly reduce the mechanical properties of the formed specimens. The main challenge for this technology is how to prevent defects from improving the mechanical properties of mechanical parts [5–14].

With exceptional tissue stability, good toughness, plasticity, and high-temperature deformation capabilities, Ti-6Al-4V is a two-phase alloy made of [15]. Compared to wrought titanium alloys, the most apparent difference in titanium alloy parts formed by additive manufacturing is that their mechanical properties are less affected by the inclusion of rigid inclusions in the microstructure, the amount of α controlling the maximum dislocation slip of the grains, and other factors [16]. The main reasons affecting the mechanical properties of SLM-molded parts are the defects and internal stresses generated by high thermal gradients [17]. The most frequent flaws include un-melted (LOF) flaws that are brought on by an insufficient energy density [18,19], initial powder contamination, and evaporation and porosity from localized pores following powder layer deposition [20,21]. For this reason, they have been intensively investigated by scholars. Leuders et al. [22] examined TC4 samples prepared by SLM and computed tomography in three dimensions (3D) and measured their quantitative porosity, obtaining high relative density values from 99.77% to 100%. Wu studied the impact of heat behavior on molded parts [23] and colleagues. These findings

indicate that the influence of heat accumulation is the primary cause of changes in mechanical properties and fracture characteristics. Specimens with reduced build thickness had a finer grain size, stronger microhardness, and lower elongation at break, according to research by Razavi et al. [24] on the impact of forming thickness on their specimens. Xu et al. [3] found that the SLM titanium alloy, with deposited titanium, had columnar pristine β grains filled with needle-like α′ martensite, which made the material exhibit high strength. Liu et al. [25] investigated high perimeter fatigue properties and failure mechanisms and showed that the fatigue cracks of the fractured samples all sprouted from unfused defects.

In this paper, it was considered that the heat transfer gradient after the action of the heat source at the same energy density changed with an increase in the deposition thickness, which, in turn, affected the forming effect [26]. For this reason, a new forming process was proposed in which the specimens were layered according to the method of slicing software, and each slice defined an energy density. The same model was formed using different energy density-creating methods, called the variable parameter forming process (VPEP). This study used the variable parameter forming process (VPEP) method to investigate the impact law of parameter changes on its specimens. It offers new suggestions for the SLM forming structure, some data, and a theoretical research foundation for the process method of forming samples.

2. Experimental Materials and Methods

2.1. Materials

The test substance was a titanium alloy TC4 powder, which was made using the aerosolization method and provided by Feierkang Rapid Manufacturing Technology Co., Ltd. (Wuxi, China). The earliest and most popular general-purpose titanium alloy used in airplane construction was the TC4 titanium alloy: a medium-strength titanium alloy that was successfully produced in the early 1940s. It has good overall performance [27–30]. Figure 1a illustrates the powder morphology of the TC4 alloy particles. Figure 1b depicts the powder's particle size distribution, which ranges from 15 μm to 53 μm with an average particle size of 35 μm. ICP-OES was used to determine the chemical composition of the alloy powders, and the results are displayed in Table 1. The TC4 alloy powder was put in a vacuum-drying oven before the test to remove any moisture that might have been adsorbed on the surface.

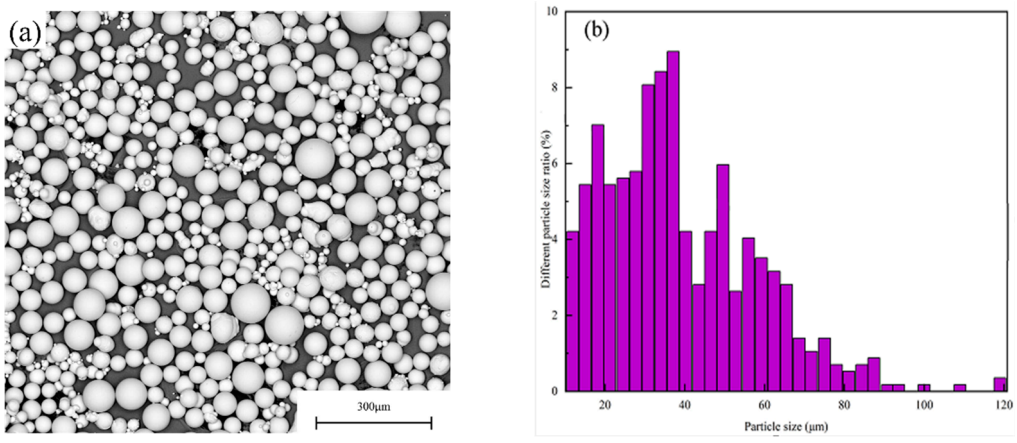


Figure 1. The TC4 powder's microstructure and particle size distribution. (**a**) Morphology of powder; (**b**) Size of powder particle percentage.

Table 1. TC4 titanium alloy powder chemical compositions.

Element	Ti	Al	V	Fe	C	N	H	O
Wt.%	Balance	5.5~6.5	3.5~4.5	0.25	0.08	0.03	0.0125	0.13

2.2. Test Equipment

The test setup consisted of a Renishaw AM 400 metal 3D printer with a maximum power of 400 W, as shown in Figure 2. Figure 2 shows the device's internal structure and working process. Firstly, the 3D CNC model STL file of the sample part was imported into the computer control software system of the SLM device. In the metal printer compartment, the powder spreader first spread a certain thickness of the metal powder. The 3D printer used a laser to provide an energy heat source that irradiated the metal powder through an oscillating mirror, causing the layers of the metal powder to melt according to a specific scan path. After forming a layer, the substrate dropped a layer of powder at height with the elevator, the powder spreader spread the powder again, and the laser started scanning again. The metal powder, after being checked, melted and formed a metallurgical bond with the previous layer and was built up layer by layer to create the final specimen that met the requirements. The machine operated in a continuous pulsed laser mode using an Nd: YAG laser with a beam diameter of 70 microns, which was capable of processing parts up to 250 mm. Argon must be used as a protective gas to fill the workspace, creating a closed environment with oxygen levels below 200 ppm.

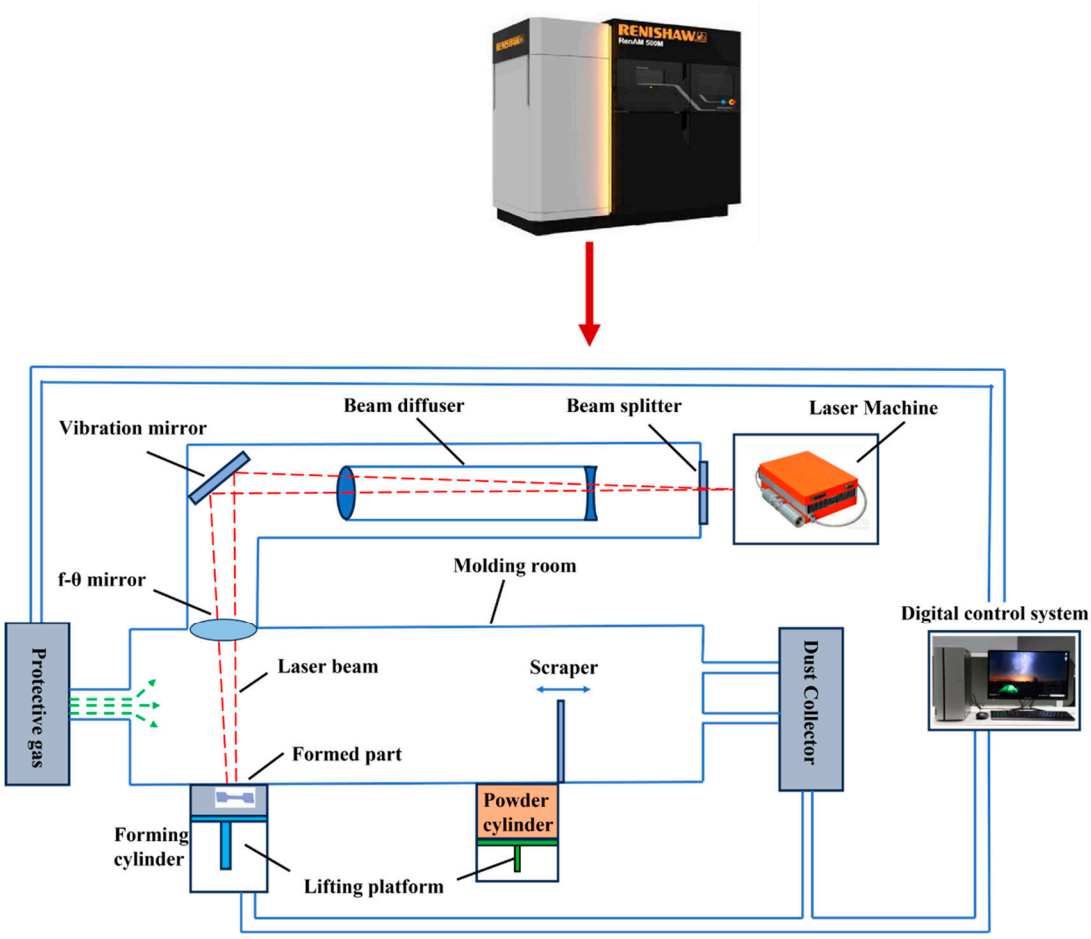


Figure 2. RENISHAW AM400 and its working process.

2.3. Process and Method

As the laser beam moved away from the point of action, the powder rapidly melted to form a molten pool. A larger melt pool could promote microstructural changes by increasing the temperature gradient, and this affected the mechanical properties. The following process parameters were chosen for this experiment: a point distance of 35 m, an exposure time of 80 s, a line distance of 0.07 mm, laser power, and layer distribution, as shown in Table 2.

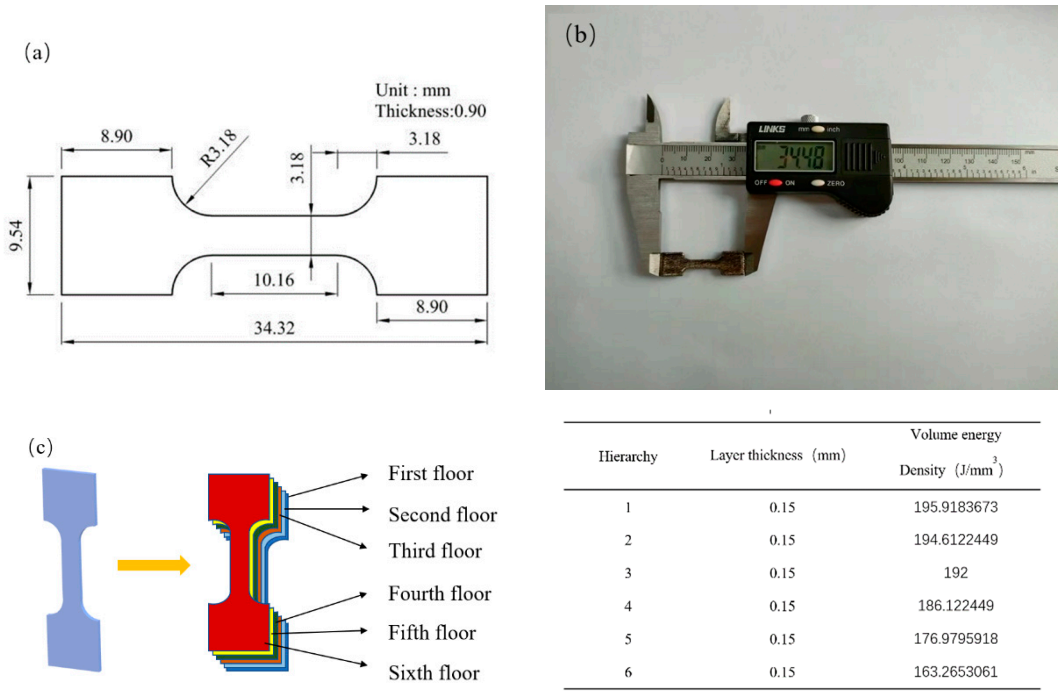
Table 2. Experimental parameters.

Number of Specimens	Number of Hierarchy	Layer Thickness (mm)	Aggregate Thickness (mm)	Laser Power per Hierarchy (W)					
				1	2	3	4	5	6
S1	6	0.15	0.9	300	298	294	285	271	250
S2	6	0.15	0.9	300	296	289	279	266	250
S3	6	0.15	0.9	300	290	280	270	260	250
S4	6	0.15	0.9	300	286	275	266	257	250
S5	6	0.15	0.9	300	284	273	264	257	250

Figure 3a shows the geometry of the tensile part with a thickness of 0.9 mm, and Figure 3b shows the actual printed tensile specimen. The specimen's process parameters are expressed in terms of energy density, and the volumetric energy density is as follows:

$$E = \frac{P}{vht} \tag{1}$$

where E denotes the volume energy density, P denotes laser power, v denotes the laser scanning speed, h denotes scan line spacing, and t denotes the layer thickness.



Hierarchy	Layer thickness (mm)	Volume energy Density (J/mm^3)
1	0.15	195.9183673
2	0.15	194.6122449
3	0.15	192
4	0.15	186.122449
5	0.15	176.9795918
6	0.15	163.2653061

Figure 3. Six hierarchies of tensile parts, each with a different size and density distribution. (**a**) Dimensions of the tensile components; (**b**) Constructing samples; (**c**) Six hierarchies of tensile parts' physical density distribution.

In order to further study the specimens formed by the variable reference forming process, different functions were used for the selected parameters of the regional pieces in the same number of layers and the same range of laser power parameters, and the expressions of the functions are shown below:

$$y = a - bn^x \tag{2}$$

In Formula (2), a and b are constants; y represents the laser power, n represents the layer level, and x represents the power exponent.

In the experimental parameter design, x could be taken as 3, 2, 1, 1/2, 1/3. The results were calculated as follows: (Equation (3) for the change function of the test piece S1, Equation (4) for the change function of the test piece S2, Equation (5) for the change function of the test piece S3, Equation (6) for the change function of the test piece S4, and Equation (7) for the change function of the test piece S5). Figure 4 exhibits the relationship between the layers of the experimental design and the laser power.

$$y_5 = 300.23 - 0.23n^3 \quad (3)$$

$$y_4 = 301.42 - 1.42n^2 \quad (4)$$

$$y_1 = 310 - 10n \quad (5)$$

$$y_2 = 334.51 - 34.51\sqrt{n} \quad (6)$$

$$y_3 = 361.21 - 61.21\sqrt[3]{n} \quad (7)$$

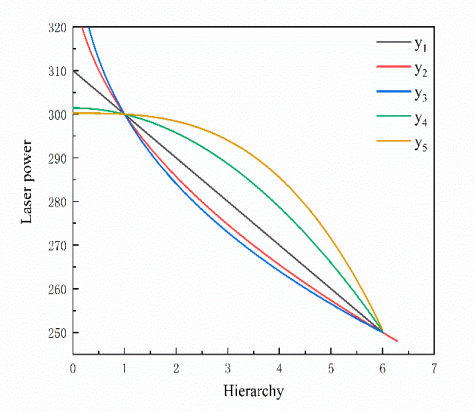


Figure 4. Level and laser power change trend.

2.4. Characterization

The specimens were tested using a UTM5305 electronic universal material testing machine (Shenzhen, China) (Figure 5) for the room temperature tensile test at 0.6 mm/min per GB/T228-2002. The same sample was measured three times, and the average value was taken. The load and deformation were recorded during the tensile process, the stress–strain curve was calculated and plotted, and the tensile strength and yield strength were obtained. The Kroll reagent was used to erode the surface of the test piece after grinding and polishing, and first wiped, the metal surface with degreasing cotton soaked with a corrosive solution for 2 min. When the metal surface showed a dark pink color, it washed off the residual Kroll reagent on the surface of the specimen with ionized water and finally rinsed and blow-dried the cover with alcohol. The microstructure patterns of the examples were observed using an ultra-deep field microscope (VHX-600E) and a scanning electron microscope (Phenom XL, Thermo Fisher Scientific, Shanghai, China). In this paper, the significance level α of confidence was set at 0.05 for sample measurements of sample densities; thus, the accuracy of the data could be guaranteed. For further differentiation, adjustments were made in the article, and the values were adjusted to retain two decimal places.



Figure 5. UTM5305 electronic universal testing machine.

3. Results and Discussion

3.1. Densitometric Analysis

Figure 6 shows the densities of the specimens with different trends in the same parameter interval. In this experiment, the samples' densities were assessed using the Archimedes' drainage technique. Each sample was tested three times, and the average value served as the density value in the following calculation to determine how compact the sample was (8).

$$\theta = \left\{ \frac{M \Big/ \left[\frac{M_1 - M_0}{\rho_0} \right]}{\rho_1} \right\} \times 100\% \tag{8}$$

where θ is the dense density; M is the mass of the TC4 sample, g; M_1 is the total mass of the TC4 sample and the water immersed in water, g; M_2 is the mass of water, g; ρ_0 is the density of water, g/cm^3; ρ_1 is the standard density of the TC4 titanium alloy, g/cm^3. (TC4 titanium alloy standard density: 4.5 g/cm^3 [31]).

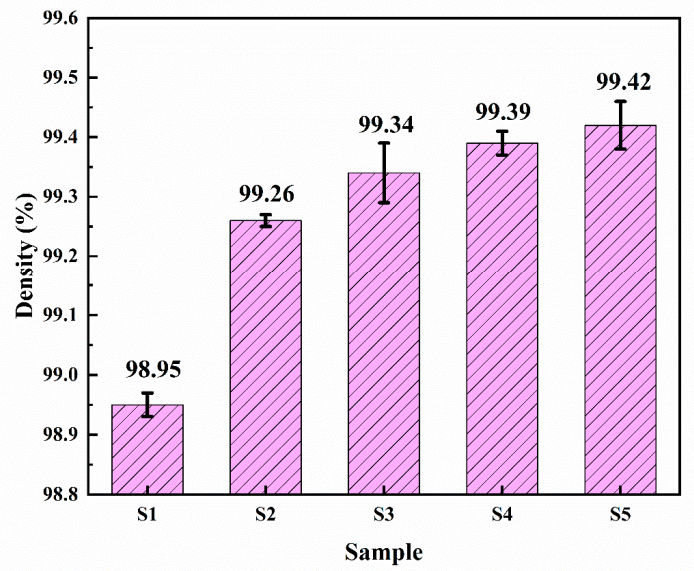


Figure 6. Density measurements of the specimen's results.

From the results, it could be seen that the values of the densities of the specimens increased with the decrease in the power exponent and leveled off with the changes under different trends. The internal forming quality significantly affected the specimen's density during the specimen-forming process. Generally speaking, internal flaws like holes, cracks, and un-melted layers significantly impacted the specimen's density. The parameters used in this experiment were made with preliminary screening, and the obtained specimens had a low occupancy of internal pores and interlayer infusion. Therefore, internal cracks were the main reason for the size of the densities of the specimens in this experiment. In the trend of different models, as the power index decreased, that is, the samples in the forming process and the high-power parameters of forming caused by internal cracks meant that the difference between the parameters of the layers gradually decreased. Then the internal cracks gradually became smaller; therefore, the denseness of the specimens gradually increased.

3.2. Surface Roughness Analysis

In total, 8 mm × 8 mm of each sample was chosen for a roughness inspection. Figure 7 depicts the specimen's surface roughness as measured by an ASI SZ-02000 auto stereo zoom microscope. It could be observed that as the power index decreased, the denseness of the specimen became smaller, and the surface-forming quality of the model was better. From Figure 7e, it is noteworthy that the densities of the specimens reached 21.9 µm when the power index was 1/3. The surface roughness was a test piece in the forming process showing a cumulative effect; that is, the quality of the last layer of forming received the influence of the layer formed in front. When the laser acted on a thicker powder layer, the melt pool formed larger metal droplets, which were subject to surface tension and created a higher surface morphology. This phenomenon also led to discontinuity in the lapping rate of adjacent scanned and formed dots and lines and even spalling, which affected the surface roughness of the specimen. In Figure 7a, the spalling area is more extensive, thus affecting the surface morphology. Table 3 demonstrates other parameters on the surface roughness of the samples. S_p represents the height between the highest peak jade mean plane, S_v represents the height between the deepest valley and the mean plane, and S_z is between the highest peak and the deepest valley. It can be seen from Table 3 that sample S1 had an enormous S_p and S_v of 64.3 µm and 54.2 µm, respectively. Sample S5 had the smallest S_p and S_v of 30.2 µm and 40.5 µm, respectively. The gradual decrease in S_p and S_v from sample S1 to sample S5 eventually reduced the average roughness S_a for each sample.

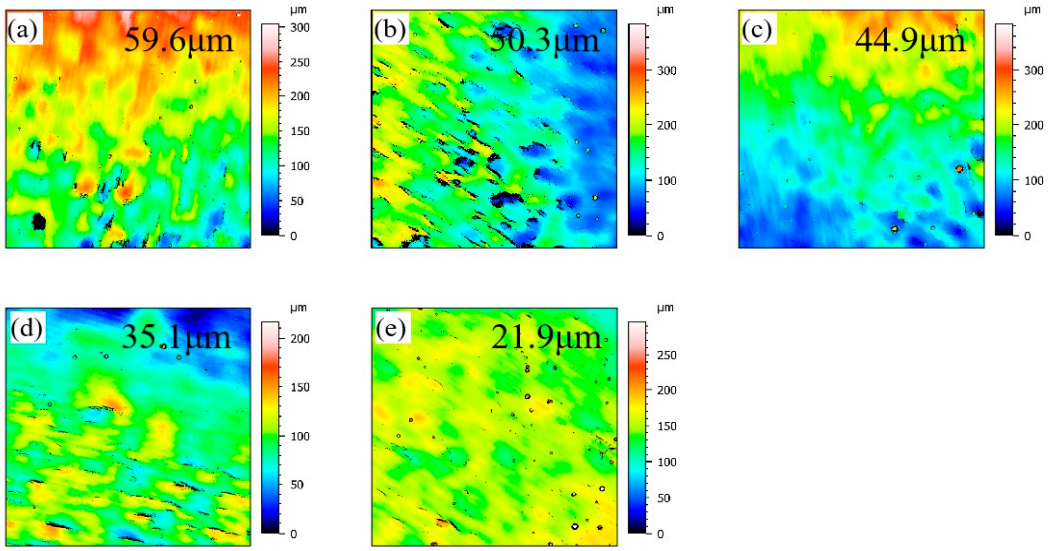


Figure 7. The surface roughness of the specimen. (**a**) S1; (**b**) S2; (**c**) S3; (**d**) S4; (**e**) S5.

Table 3. Sample surface roughness.

Samples	S_a/μm	S_p/μm	S_v/μm	S_z/μm
S1	59.6	64.3	54.2	119
S2	50.3	56.3	45.6	102
S3	44.9	50.1	39.8	90
S4	35.1	41.3	44.3	86
S5	21.9	30.2	40.5	71

3.3. Surface Hardness Analysis

The measurement of Vickers hardness for the formed specimens used a fully automatic micro Vickers hardness tester (TIME 6610AT). The surface was smoothed before the measurement; the measuring pressure was 1000 N, the holding time was 15 s, and the spacing between each measuring point was more significant than 0.3 mm. Each specimen was measured for five consecutive RMS values, and the average value was taken. Figure 8 depicts the measured values of the surface hardness of the examples. These specimens had similar surface hardness values; their maximum moderate hardness was 411.10 HV. The change in energy density between the layers had a negligible effect on the hardness of the specimen, with a maximum difference of 3 HV. Since the variable reference forming process was performed at the same range of laser power, the difference in temperature gradients during the thermoforming process was negligible. Therefore, the hardness difference in the specimens with variable reference forming was insignificant. The surface layers of the specimen were formed using the same parametric technique; therefore, the surface roughness of the top layer was affected by the surface roughness of the bottom layer. The laser action on the loose powder and the formed specimen caused a difference in the volume of the formed melt pool, resulting in a different porosity on the formed surface, which, to some extent, affected the surface hardness of the specimen. When employing the variable reference molding method, the energy parameters of the highest surface could be changed for specimens with high surface hardness requirements to increase the surface hardness of the model.

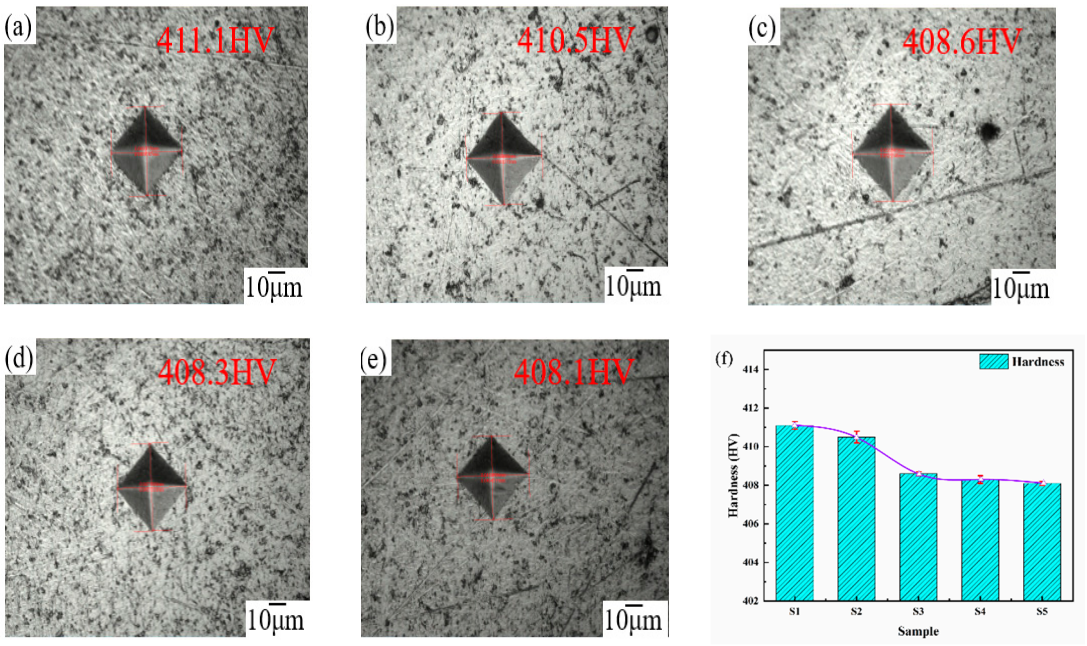


Figure 8. Surface hardness of the specimen. (**a**) S1; (**b**) S2; (**c**) S3; (**d**) S4; (**e**) S5. (**f**) The trend of the overall hardness of the sample.

The surface molding quality of the specimen could be determined by examining the surface morphology and surface roughness. The surface molding quality of the upper layer impacted the uniformity of the spreading powder on the subsequent layer of the specimen. Working with the same laser energy, different layer thicknesses affected the forming quality of the sample, especially on the surface. The testing results revealed that while there was no discernible variation in the surface hardness of the specimens, the surface roughness of the samples reduced as the power index declined.

3.4. Analysis of Tensile Properties

Table 4 shows the tensile strength, yield strength, and elongation for different trends in the variable reference molding process. In this test, the mechanical properties of the specimens were formed using the variable-reference forming process, which was much more significant than those of the solid-reference formed specimens. The minimum tensile strength of this variable reference-creating illustration could reach 1034.92 MPa, and the minimum yield strength came to 959.45 MPa. Because the variable reference forming process gradually reduced the energy density during the forming process, there was substantially less energy penetration in the remelted layer into the deposited layer than there was with the solid reference forming a circle. As a result, there were fewer thermal cracks in the deposited layers, and the tensile and yield strengths of the specimens improved. The variable reference molding process improved the specimen's internal defects and increased the example's tensile strength. For models formed by the variable reference developing process, the smaller the difference in the laser power between the layers, the greater the specimens' tensile strength. The elongation of individual specimens had no apparent pattern, and the maximum extension reached 5.95%. Changing references could successfully increase the density, decrease the internal stress concentration, and increase the tensile strength of the specimen. The specimen's tensile strength gradually rose as the power index declined. The degree of crystallinity somewhat determined the tensile strength [32,33]. The internal grains of the specimens formed by the variable reference process were smaller. Therefore, the grain surface had a larger surface, which improved the reactivity and strength of the material. At the same time, the grain distribution of variable reference forming was more uniform, which reduced the number and length of the grain boundaries, thus reducing the defects and strength differences of the material. The material elongation was influenced by grain size and uniformity [34,35]. When the layer energy density index was three, the laser energy density produced temperatures outside the optimal temperature range for TC4 plasticity, resulting in grain distribution changes and lower elongation than that of the other specimens.

Table 4. Tensile properties of formed parts with variable reference.

Samples	σ_b/MPa	$\sigma_{0.2}$/MPa	Elongation %
S1	1034.92	959.45	4.90
S2	1144.90	1061.36	4.85
S3	1160.23	1075.67	5.51
S4	1164.24	1091.28	5.95
S5	1190.84	1103.87	4.61

3.5. Fracture Morphology Analysis

The fracture keeps track of every detail relating to the fracture, including the crack's emergence, growth, and eventual failure. In conclusion, several internal and external elements, including fracture mechanics and fracture physics, contributed to the diverse fracture information on the fracture. Strong evidence for determining the fracture failure mode and hints for diagnosing the cause of fracture failure was provided by the qualitative and quantitative investigation of the fracture. The fracture morphology of the TC4 titanium alloy could be observed using scanning electron microscopy, and the specimens created by various processes could also be examined using this method.

Figure 9 shows the fracture morphology of the specimens after stretching with different variable reference forming. Deep equiaxed challenging nests dominated the fracture morphology, and all fracture mechanisms indicated a ductile fracture. Figure 9a shows the fracture morphology of the S1 specimen after stretching. It could be observed that there were more hole defects on the fracture surface, which was mainly because the gradient of the layer and energy density was not reasonable, resulting in more air residue during the forming process, and the hole defects led to a stress concentration, thus reducing the tensile strength of the formed specimen. Figure 9b–e shows the fracture morphology of specimens S2, S3, S4, and S5 after stretching, respectively. Usually, many micropores exist around the fracture, which is irregular in form and inconsistent in size. During the tensile process of the specimen, the faster strain rate leads to stress concentration from the dislocation slip, and the micro-pores are subjected to forces that fracture and form challenging nests around the cluster of holes [36]. The stress concentration generated around the micropores can lead to crack generation and expansion, and the surface of the fracture has traces of cracks extending along the fracture. It is important to note that as the exponential power decline in the ply energy density occurs, the quantity and size of holes in the superficial tensile cracks decrease. In the vicinity of the specimen S5 surface tensile fracture, there were only a few microporous defects as opposed to many huge holes. This had a minor impact on the mechanical characteristics of the specimen, and the fracture surface was comparatively flat.

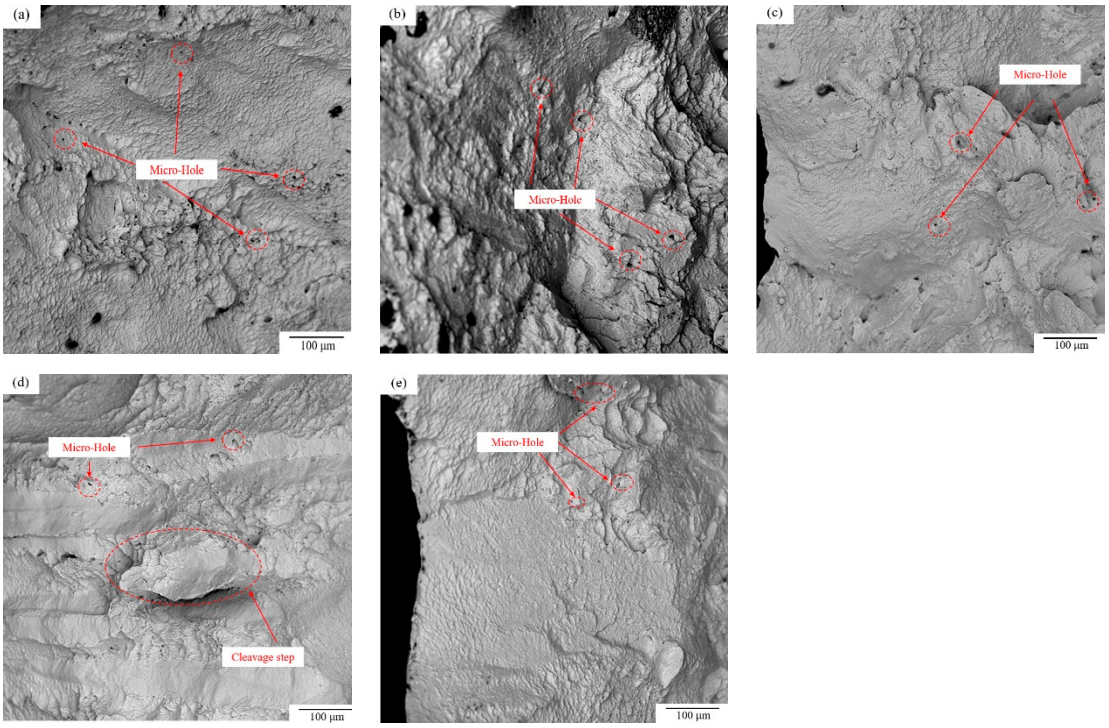


Figure 9. The tensile fracture morphology of specimens formed by various processes. (**a**) S1; (**b**) S2; (**c**) S3; (**d**) S4; (**e**) S5.

3.6. Microstructure Analysis

Following the predetermined layer energy density, Figure 10 depicts the optical microstructure of the tensile section after crystal grinding and polishing corrosion with a laser power of 300–250 W, which was separated into six layers. Figure 10a demonstrates that the dark phase was spread along the grain boundary and that the bright white portion of the matrix phase made up most of the cladding layer. The needle-like martensite α' within the β-phase of the columnar crystal intersected and nucleated at the boundary of the β-phase of the columnar crystal. Three main phase transitions occurred in TC4 titanium alloys during laser cladding: isotropic transition/ordering transition and co-precipitation transition. The

isomeric transformation occurred mainly at high temperatures and was a transformation of the unstable β-phase α-phase: a process controlled primarily by the diffusion of vanadium elements [37,38]. The ordered transformation generated ordered phases such as Ti_3Al, and the co-precipitation transformation was mainly the decomposition of the unstable β-phase. During the heating process, the diffusion of V elements in TC4 led to the dissolution of α in β; hexagonal martensite (α′) was formed at a fast-cooling rate (>410 K/s), the Weiss-phase (α_m) was formed at a medium cooling rate (20~410 K/s). The primary phase (α_p) and residual β phase coexisted in titanium at a slow cooling rate (<20 K/s). When the heating temperature was lower than the β phase transition temperature, the α phase dissolved during the heating process to generate the primary phase αp, and the second phase (α_s) was generated from the β phase during cooling, forming a state where α_s, α_p, and β coexisted [37,38]. As shown in Figure 10b–f, it illustrated that the microstructure α′ of the specimens prepared by the variable-reference forming process was influenced more by the energy gradient of the last layers. The aspect ratio of the primary α′ on the surface of the specimens decreased with the increase or the decrease in the energy density of each layer. The number of secondary α′ decreased. The low energy density of the post-deposited layer body affected the cooling rate of the specimen and, thus, the number of secondary phase α_s generated from the β-phase.

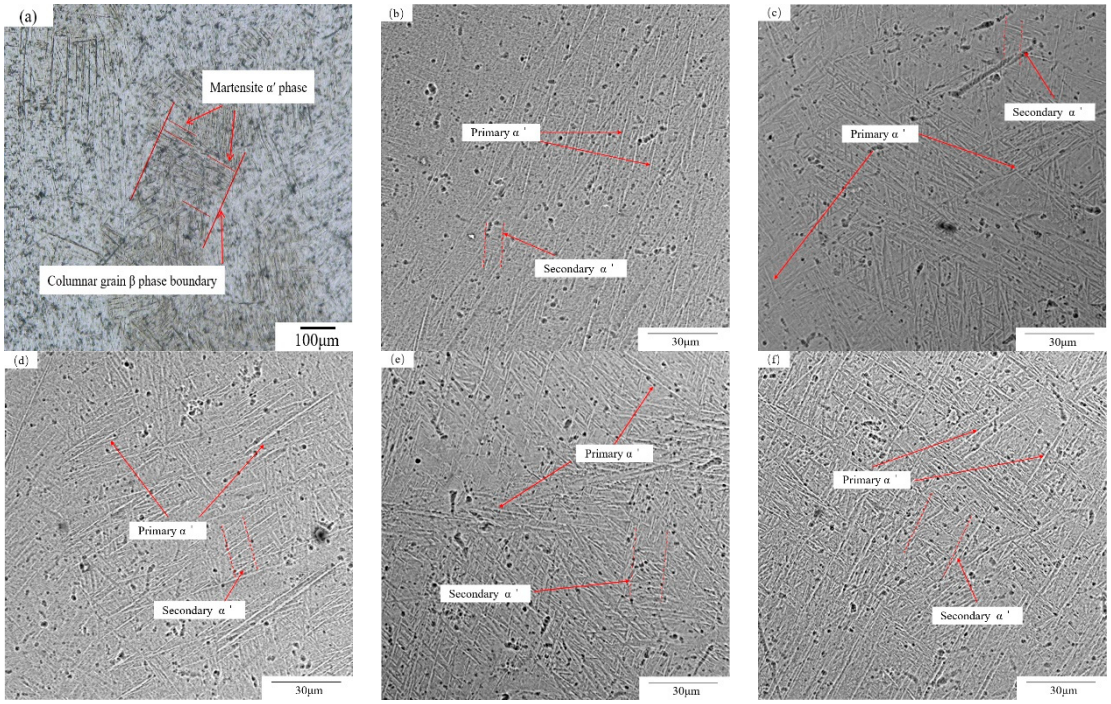


Figure 10. Microstructure images. (**a**) Microscopic images in light; (**b**) SEM image of sample S1; (**c**) SEM image of sample S2; (**d**) SEM image of sample S3; (**e**) SEM image of sample S4; (**f**) SEM image of sample S5.

3.7. Discussion

Through the above analysis, the density and tensile strengths of the specimens in the variable-reference molding process were better than those of the solid-reference molding process, which also showed that the representatives changed with layer thickness during the molding process. The trend of the parameters changing during the molding process became more and more stable, as can be seen from the test of the actual change in the variable-reference molding process.

1. When the specimen was formed in the initial layer, the sample needed to be better bonded with the substrate. A higher process temperature could increase the melted

pool and increase the bonding of the model with the substrate. The higher process temperature ensured better molding of the city and reduced the risk of warping the unformed specimen.

2. High energy density during the specimen-forming process resulted in flaws such as internal cracks and spattering. By contrast, low energy density resulted in the powder not fusing, leading to deficiencies like interlayer un-melted, etc. The solid reference forming process test revealed that when the laser power was 250 W, the upper layer of the produced specimen had fewer internal faults, demonstrating the superiority of the chosen process parameters. There were differences between the processes used to generate the bottom layer and the higher surface layer.
3. Through the analysis in parts (1) and (2), it was determined that the bottom layer needed a more significant energy density, and the upper layer needed a smaller energy density relative to the bottom layer during the forming process of the specimen, as shown in schematic 11. In this study, by selecting the laser power of 300 W for the bottom layer and 250 W for the uppermost layer, the process parameters of the upper surface layer and the lower layer had different values by exploring the trend of changes in them. The experimental results found that the specimens' forming quality tended to be stable during the forming process of SLM specimens. The main factors affected included the concentration of oxygen and the initial processing of the specimen because the highest content of oxygen concentration was controlled in the forming chamber. However, there was still a certain amount of oxygen in the process of gradually forming the specimen; oxygen was slowly consumed, and the subsequent forming layer was steadily stabilized in relation to the initial layer. Figure 11c,d shows the ratio of the elemental content at the bottom and top of the same specimen, and it could be seen that the oxygen content at the top of the model was significantly reduced. The second was the effect under condition (1). The third was the surface height error of the substrate at the time of forming the initial layer of the test piece; the initial layer of the processing powder layer height was nonuniform, and there was no such problem in the subsequent layer.

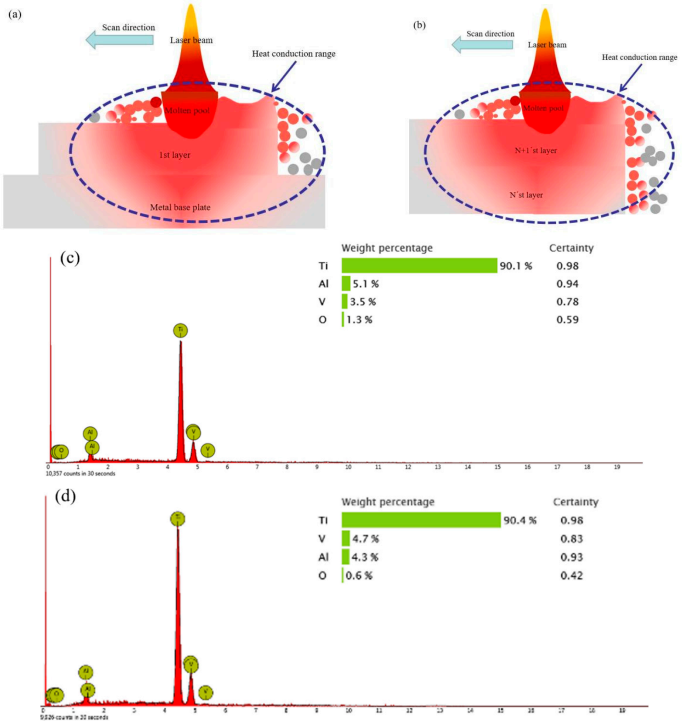


Figure 11. Temperature ranges for various molding heights. (**a**) Temperature range of metal base plate forming propagation; (**b**) The specimen-forming process's temperature propagation range;

(**c**) Proportion of elemental content in the bottom layer of the specimen; (**d**) Proportion of elemental content in the top layer of the specimen.

4. Conclusions

In this study, the surface forming quality of the specimens and the tensile properties of the specimens were investigated by exploring different variation trends at the same ply level, and the main findings were as follows:

1. The densities of the specimens increased as the power index decreased, with the highest densities reaching 99.42%.
2. The surface quality of the formed specimen was also affected by the trend in the variable reference forming process, with the process influencing surface roughness but not surface hardness.
3. The tensile strength of the specimen increased as the power index decreased, reaching a maximum of 1190.84 MPa and a maximum yield strength of 1103.87 MPa.
4. The variable parameter forming process could reduce some defects caused by the forming process of the specimen and, at the same time, could reflect the state of SLM forming, i.e., the specimen became more and more stable with the high layer height, and the forming parameters tended to be the parameters of the stable state; in this experiment, the parameters of the designed state specimen with a power index of 1/3 had a better comprehensive performance.

Author Contributions: J.H.: Conceptualization, Resources, Investigation, Methodology, Formal analysis, Writing—original draft, Writing—review & editing. S.J.: Validation, Writing, Writing—original draft, Reviewing and Editing, Writing—review & editing. Y.L. (Yude Liu): Conceptualization, Investigation, Validation, Visualization, Writing—Original draft, Resources. W.S.: Conceptualization, Investigation, Validation, Visualization, Writing—Original draft, Resources. Y.Z.: Conceptualization, Investigation, Validation, Visualization. Y.L. (Yuxiang Lin): Conceptualization, Investigation, Validation, Visualization. J.L.: Conceptualization, Investigation, Validation, Visualization. Y.H.: Conceptualization, Investigation, Validation, Visualization. All authors have read and agreed to the published version of the manuscript.

Funding: The financial supports provided by grants National Key Research and Development Program of China (2022YFC2406004), the National Natural Science Foundation of China (51975006; 51505006), and the Research Foundation for Youth Scholars of Beijing Technology and Business University are greatly appreciated.

Data Availability Statement: Data is contained within the article.

Conflicts of Interest: The authors declare no conflict of interest.

References

1. Gu, D.; Shi, X.; Poprawe, R.; Bourell, D.L.; Setchi, R.; Zhu, J. Material-structure-performance integrated laser-metal additive manufacturing. *Science* **2021**, *372*, eabg1487. [CrossRef] [PubMed]
2. Ren, D.C.; Zhang, H.B.; Liu, Y.J.; Li, S.J.; Jin, W.; Yang, R.; Zhang, L.C. Microstructure and properties of equiatomic Ti–Ni alloy fabricated by selective laser melting. *Mater. Sci. Eng. A* **2020**, *771*, 138586. [CrossRef]
3. Xu, W.; Brandt, M.; Sun, S.; Elambasseril, J.; Liu, Q.; Latham, K.; Xia, K.; Qian, M. Additive manufacturing of strong and ductile Ti–6Al–4V by selective laser melting via in situ martensite decomposition. *Acta Mater.* **2015**, *85*, 74–84. [CrossRef]
4. Zhang, L.C.; Liu, Y.; Li, S.; Hao, Y. Additive manufacturing of titanium alloys by electron beam melting: A review. *Adv. Eng. Mater.* **2018**, *20*, 1700842. [CrossRef]
5. Vrancken, B.; Thijs, L.; Kruth, J.-P.; Van Humbeeck, J. Heat treatment of Ti6Al4V produced by Selective Laser Melting: Microstructure and mechanical properties. *J. Alloys Compd.* **2012**, *541*, 177–185. [CrossRef]
6. Maskery, I.; Aboulkhair, N.T.; Aremu, A.O.; Tuck, C.J.; Ashcroft, I.A.; Wildman, R.D.; Hague, R.J.M. A mechanical property evaluation of graded density Al-Si10-Mg lattice structures manufactured by selective laser melting. *Mater. Sci. Eng. A* **2016**, *670*, 264–274. [CrossRef]
7. Deshpande, A.; Deb Nath, S.; Atre, S.; Hsu, K. Effect of Post Processing Heat Treatment Routes on Microstructure and Mechanical Property Evolution of Haynes 282 Ni-Based Superalloy Fabricated with Selective Laser Melting (SLM). *Metals* **2020**, *10*, 629. [CrossRef]

8. Hu, X.; Xue, Z.; Zhao, G.; Yun, J.; Shi, D.; Yang, X. Laser welding of a selective laser melted Ni-base superalloy: Microstructure and high temperature mechanical property. *Mater. Sci. Eng. A* **2019**, *745*, 335–345. [CrossRef]
9. He, B.; Wu, W.; Zhang, L.; Lu, L.; Yang, Q.; Long, Q.; Chang, K. Microstructural characteristic and mechanical property of Ti6Al4V alloy fabricated by selective laser melting. *Vacuum* **2018**, *150*, 79–83. [CrossRef]
10. Chang, K.; Liang, E.; Huang, W.; Zhang, X.; Chen, Y.; Dong, J.; Zhang, R. Microstructural feature and mechanical property in different building directions of additive manufactured Ti6Al4V alloy. *Mater. Lett.* **2020**, *267*, 127516. [CrossRef]
11. Lu, Y.; Wu, S.; Gan, Y.; Huang, T.; Yang, C.; Junjie, L.; Lin, J. Study on the microstructure, mechanical property and residual stress of SLM Inconel-718 alloy manufactured by differing island scanning strategy. *Opt. Laser Technol.* **2015**, *75*, 197–206. [CrossRef]
12. Hanzl, P.; Zetek, M.; Bakša, T.; Kroupa, T. The influence of processing parameters on the mechanical properties of SLM parts. *Procedia Eng.* **2015**, *100*, 1405–1413. [CrossRef]
13. Simonelli, M.; Tse, Y.Y.; Tuck, C. Effect of the build orientation on the mechanical properties and fracture modes of SLM Ti–6Al–4V. *Mater. Sci. Eng. A* **2014**, *616*, 1–11. [CrossRef]
14. Leary, M.; Mazur, M.; Williams, H.; Yang, E.; Alghamdi, A.; Lozanovski, B.; Zhang, X.; Shidid, D.; Farahbod-Sternahl, L.; Witt, G.; et al. Inconel 625 lattice structures manufactured by selective laser melting (SLM): Mechanical properties, deformation and failure modes. *Mater. Des.* **2018**, *157*, 179–199. [CrossRef]
15. Boyer, R.R. An overview on the use of titanium in the aerospace industry. *Mater. Sci. Eng. A* **1996**, *213*, 103–114. [CrossRef]
16. Benedetti, M.; Fontanari, V.; Bandini, M.; Zanini, F.; Carmignato, S. Low-and high-cycle fatigue resistance of Ti-6Al-4V ELI additively manufactured via selective laser melting: Mean stress and defect sensitivity. *Int. J. Fatigue* **2018**, *107*, 96–109. [CrossRef]
17. Fergani, O.; Berto, F.; Welo, T.; Liang, S.Y. Analytical modelling of residual stress in additive manufacturing. *Fatigue Fract. Eng. Mater. Struct.* **2017**, *40*, 971–978. [CrossRef]
18. Liu, Q.C.; Elambasseril, J.; Sun, S.J.; Leary, M.; Brandt, M.; Sharp, P.K. The effect of manufacturing defects on the fatigue behaviour of Ti-6Al-4V specimens fabricated using selective laser melting. In *Advanced Materials Research*; Trans Tech Publications Ltd.: Stafa-Zurich, Switzerland, 2014; Volume 891, pp. 1519–1524.
19. Wycisk, E.; Solbach, A.; Siddique, S.; Herzog, D.; Walther, F.; Emmelmann, C. Effects of defects in laser additive manufactured Ti-6Al-4V on fatigue properties. *Phys. Procedia* **2014**, *56*, 371–378. [CrossRef]
20. Vilaro, T.; Colin, C.; Bartout, J.D. As-fabricated and heat-treated microstructures of the Ti-6Al-4V alloy processed by selective laser melting. *Metall. Mater. Trans. A* **2011**, *42*, 3190–3199. [CrossRef]
21. Gorny, B.; Niendorf, T.; Lackmann, J.; Thoene, M.; Troester, T.; Maier, H.J. In situ characterization of the deformation and failure behavior of non-stochastic porous structures processed by selective laser melting. *Mater. Sci. Eng. A* **2011**, *528*, 7962–7967. [CrossRef]
22. Leuders, S.; Thöne, M.; Riemer, A.; Niendorf, T.; Tröster, T.; Richard, H.A.; Maier, H.J. On the mechanical behaviour of titanium alloy TiAl6V4 manufactured by selective laser melting: Fatigue resistance and crack growth performance. *Int. J. Fatigue* **2013**, *48*, 300–307. [CrossRef]
23. Wu, B.; Pan, Z.; Ding, D.; Cuiuri, D.; Li, H. Effects of heat accumulation on microstructure and mechanical properties of Ti6Al4V alloy deposited by wire arc additive manufacturing. *Addit. Manuf.* **2018**, *23*, 151–160. [CrossRef]
24. Razavi, S.M.J.; Van Hooreweder, B.; Berto, F. Effect of build thickness and geometry on quasi-static and fatigue behavior of Ti-6Al-4V produced by Electron Beam Melting. *Addit. Manuf.* **2020**, *36*, 101426. [CrossRef]
25. Liu, L.; Zhang, Z.J.; Yang, H.J.; Ji, H.B.; Chen, J.; Yi, J.L.; Wang, L.; Li, X.W.; Zhang, Z.F. Effect of Defects on High Cycle Fatigue Property of Selective Laser Melted Ti6Al4V Alloy. *Rare Met. Mater. Eng.* **2022**, *50*, 4429–4436.
26. Liu, Y.; Zhou, Y.; Shi, W.; Han, J.; Ye, D.; Han, Y. Experimental Research on Variable Parameter Forming Process for Forming Specimen of TC4 Titanium Alloy by Selective Laser Melting. *Materials* **2022**, *15*, 6408. [CrossRef]
27. Liu, W. Study on microstructure and tensile properties of TC4-DT titanium alloy forgings. *Heavy Cast. Forg.* **2018**, *3*, 38.
28. Ren, Y.M.; Lin, X.; Fu, X.; Tan, H.; Chen, J.; Huang, W.D. Microstructure and deformation behavior of Ti-6Al-4V alloy by high-power laser solid forming. *Acta Mater.* **2017**, *132*, 82–95. [CrossRef]
29. Ren, D.; Li, S.; Wang, H.; Hou, W.; Hao, Y.; Jin, W.; Yang, R.; Misra, R.D.K.; Murr, L.E. Fatigue behavior of Ti-6Al-4V cellular structures fabricated by additive manufacturing technique. *J. Mater. Sci. Technol.* **2019**, *35*, 285–294. [CrossRef]
30. Schmidt, A.M.; Azambuja, D.S. Corrosion behavior of Ti and TI6Al4V in citrate buffers containing fluoride ions. *Mater. Res.* **2010**, *13*, 45–50. [CrossRef]
31. Huang, W.; He, D.; Wang, H.; Qin, S.; Wang, L.; Xu, X. The effect of heat treatment on the anisotropy of Ti-6Al-4V by selective laser melting. *JOM* **2022**, *74*, 2724–2732. [CrossRef]
32. Nie, Y.; Dong, L.; Wu, J.; Li, D. A design of Ti-6Al-4V/ZrB2 multilayers with good thermal stability to enhance mechanical properties of titanium alloy. *Ceram. Int.* **2018**, *44*, 4704–4710. [CrossRef]
33. Al-Sayed, S.R.; Samad, F.A.; Mohamed, T.; Youssef, D. Novel Surface Topography and Microhardness Characterization of Laser Clad Layer on TC4 Titanium Alloy Using Laser-Induced Breakdown Spectroscopy and Machine Learning. *Metall. Mater. Trans.* **2022**, *53*, 3639–3653. [CrossRef]
34. Quan, G.H.; Zhao, X.Y. Study on the Influence of Process Parameters on Grain and Phases of TC4 Ti-alloy Forging. In Proceedings of the 2nd Annual International Conference on Advanced Material Engineering (AME 2016), Wuhan, China, 15–17 April 2016; Atlantis Press: Dordrecht, The Netherlands, 2016; pp. 329–333.

35. Liu, Y.; Yin, Z.; Zhu, J. Effects of Temperature, Stress and Grain Size-on Stress Relaxation in the Alloy TC 4. *Xiyou Jinshu Cailiao Yu Gongcheng Rare Met. Mater. Eng.* **2003**, *32*, 643–646.
36. Wang, S.L.; Zhang, Q.; Qiao, E.L.; Gu, Z.M.; Tian, P.F. Effects of Annealing Temperatures on Microstructure and Mechanical Properties of TC4 Titanium Alloy. *Heat Treat.* **2023**, *38*, 33–36.
37. Ahmed, T.; Rack, H.J. Phase transformations during cooling in $\alpha + \beta$ titanium alloys. *Mater. Sci. Eng. A* **1998**, *243*, 206–211. [CrossRef]
38. Kelly, S.M. *Thermal and Microstructure Modeling of Metal Deposition Processes with Application to Ti-6Al-4V*; Virginia Tech: Blacksburg, VA, USA, 2004.

Disclaimer/Publisher's Note: The statements, opinions and data contained in all publications are solely those of the individual author(s) and contributor(s) and not of MDPI and/or the editor(s). MDPI and/or the editor(s) disclaim responsibility for any injury to people or property resulting from any ideas, methods, instructions or products referred to in the content.